Metal-organic framework membranes with single-atomic centers for photocatalytic CO2 and O2 reduction

Yuchen Hao
Beijing Institute of Technology
Li-Wei Chen
Beijing Institute of Technology
Jiani Li
Beijing Institute of Technology
Yu Guo
Peking University https://orcid.org/0000-0001-5251-0377
Xin Su
Beijing Institute of Technology
Miao Shu
Shanghai Institute of Applied Physics
Qinghua Zhang
Institute of Physics, Chinese Academy of Sciences
Wen-Yan Gao
Beijing Institute of Technology
Siwu Li
Beijing Institute of Technology
Zilong Yu
Beijing Institute of Technology
Lin Gu
Beijing National Laboratory for Condensed Matter Physics, Institute of Physics, Chinese Academy of Sciences, Beijing 100190, China https://orcid.org/0000-0002-7504-031X
Xiao Feng
Beijing Institute of Technology https://orcid.org/0000-0002-3212-3051
Anxiang Yin (yin@bit.edu.cn)
Beijing Institute of Technology https://orcid.org/0000-0002-7711-7018
Rui Si
Shanghai Institute of Applied Physics
Ya-Wen Zhang
Peking University https://orcid.org/0000-0002-1871-7507

Bo Wang
Frontiers Science Center for High Energy Material, School of Chemistry and Chemical Engineering, Beijing Institute of Technology, Beijing 100081 https://orcid.org/0000-0001-9092-3252
Chun-Hua Yan
Peking University

Article

Keywords: breathable metal organic framework membranes, MOF, photocatalytic CO2 and O2 reduction, artificial photosynthesis

Posted Date: September 21st, 2020

DOI: https://doi.org/10.21203/rs.3.rs-73939/v1

Version of Record: A version of this preprint was published at Nature Communications on May 11th, 2021. See the published version at https://doi.org/10.1038/s41467-021-22991-7.

Metal-organic framework membranes with single-atomic centers for photocatalytic CO_2 and O_2 reduction

Yu-Chen Hao[1], Li-Wei Chen[1], Jiani Li[1], Yu Guo[2], Xin Su[1], Miao Shu[3], Qinghua Zhang[4], Wen-Yan Gao[1], Siwu Li[1], Zi-Long Yu[1], Lin Gu[4], Xiao Feng[1], An-Xiang Yin[1]*, Rui Si[3]*, Ya-Wen Zhang[2], Bo Wang[1,5]* and Chun-Hua Yan[2]

[1] *Ministry of Education Key Laboratory of Cluster Science, Beijing Key Laboratory of Photoelectronic/Electrophotonic Conversion Materials, School of Chemistry and Chemical Engineering, Beijing Institute of Technology, Beijing 100081, P. R. China.*

[2] *Beijing National Laboratory for Molecular Sciences, State Key Laboratory of Rare Earth Materials Chemistry and Applications, PKU-HKU Joint Laboratory in Rare Earth Materials and Bioinorganic Chemistry, College of Chemistry and Molecular Engineering, Peking University, Beijing 100871, P. R. China*

[3] *Shanghai Synchrotron Radiation Facility, Shanghai Institute of Applied Physics, Chinese Academy of Sciences, Shanghai 201204, P. R. China*

[4] *Institute of Physics, Chinese Academy of Sciences, Beijing 100190, P. R. China*

[5] *Advanced Research Institute of Multidisciplinary Science, Beijing Institute of Technology, Beijing 100081, P. R. China.*

* To whom correspondence should be addressed: yin@bit.edu.cn (A.X.Y.); sirui@sinap.ac.cn (R.S.); bowang@bit.edu.cn (B.W.)

The demand for sustainable energy has motivated the development of artificial photosynthesis. Yet the catalyst and reaction interface designs for directly fixing permanent gases into liquid fuels are still challenged by sluggish mass transfer and catalytic kinetics at the gas-liquid-solid three-phase boundary. Here, we report that breathable metal-organic framework (MOF) membranes decorated with metal single-atoms (SAs) can synergistically promote the diffusion, adsorption, and activation of gas molecules (e.g. CO_2, O_2) to boost the photocatalytic conversion of them into liquid fuels. With Ir SAs as active centers, the defect-engineered MOF (e.g. NH_2-UiO-66) matrixes can efficiently harvest visible light and sensitize the electronically tailored Ir SAs for reducing CO_2 to HCOOH with the high activity of 0.51 mmol g_{cat}^{-1} h^{-1} at the conventional three-phase reaction interface. Furthermore, the breathable SA/MOF membranes can directly convert humid CO_2 gas into HCOOH at the high-throughput gas-solid interfaces, presenting a near-unity selectivity and an unprecedented activity of 3.38 mmol g_{cat}^{-1} h^{-1}. Similarly, with Pd SAs as active centers, the SA/MOF membrane can catalyze the O_2-to-H_2O_2 conversion with an ultrahigh activity of 10.4 mmol g_{cat}^{-1} h^{-1} under visible light, suggesting the wide applicability of our catalyst and reaction interface designs.

In nature, solar energy is harnessed by photosynthesis and stored in fossil fuels through extremely slow geochemical fossilization processes. Resembling the functionalities of green leaves, interdisciplinary researchers have developed various photosynthetic systems across the natural-artificial spectrum[1–8]. Although a solar-to-electric energy conversion rate of over 20% can be achieved by inorganic photovoltaic devices[9], abiotic photosynthetic systems that can fix naturally abundant permanent gases (e.g. CO_2, O_2) into value-added liquid fuels still face challenges in productivity and selectivity[6,10]. The synergistic catalyst and reaction interface design strategy is urgently needed but not yet fully established for enabling efficient photoreduction of permanent gas at the gas-liquid-solid three-phase boundary with water as proton donors. Challenged by the large kinetic barriers, both homogeneous and heterogeneous artificial photosynthesis catalysts feature inherent advantages and trade-offs for such applications[11]. Homogeneous catalysts possess highly dispersed and accessible active sites with accurately tailored structures for specific reactions but poor product isolation and/or long-term stability[12,13]. Heterogenous approaches exhibit enhanced product separation but suffer from smaller active surface areas and limited accessibility to the active sites[14,15]. In addition, the traditional photocatalytic interface design with dissolving or submerging catalysts in aqueous solutions is optimal for reactions involving only liquid reactants (e.g. water splitting)[4]. The limited solubility and sluggish diffusion kinetics of permanent gas in aqueous solutions strongly retard the following catalytic conversion on the heterogeneous reaction interface[16–18]. In addition, the overwhelming competitions from water adsorption on the flooded catalyst surface further suppress the reduction of gas molecules with the undesired hydrogen evolution reaction (HER)[6,19,20]. Consequently, photoreduction of insoluble and stable gas molecules (e.g. CO_2, O_2) on the three-phase catalysis interface inevitably confronts three formidable challenges: (i) the kinetically hindered diffusion, (ii) the sluggish surface adsorption, and (iii) the inefficient activation and catalytic conversion of the gas reactants.

Here, we introduce leaf-like gas-permeable membranes consisting of numerous structurally tailored MOF crystals as photosensitizers and nanoreactors for three-phase artificial photosynthesis (Figure 1a). Single-atom iridium (Ir_1) and palladium (Pd_1) are anchored on the MOF nodes to serve as the catalytic hydrogenation centers for CO_2 and O_2, respectively (Figure 1b). The defect-engineering of MOF matrix can not only enhance their light harvesting capability but also tailor the chemical structures of their oxide nodes (e.g. the Zr–O notes of NH_2-UiO-66) to finely control their interactions to the introduced metal SAs. As a result, the synergy between the defect-rich Zr–O nodes and metal SAs can promote the adsorption and activation of gas reactants and efficiently convert them to specific products. Moreover, the ultrahigh porosity of SA/MOF membranes allows the creation of gas-membrane-gas (GMG) configuration, which boosts the high-throughput diffusion of humid CO_2 to the metal SAs located at the vast gas-solid reaction interfaces within the interconnected MOF pores. Compared with the traditional gas-liquid-solid reaction interface, such gas-solid interface design can significantly increase the local concentrations and molecular ratios of gas reactants (versus water) in the vicinity of each catalytic centers (e.g. SAs). Consequently, bridging advanced catalytic center and reaction interface designs, our Ir_1/*d*-aUiO membranes can

catalyze the CO_2-to-HCOOH photoreduction with near-unity selectivity and a record activity of 3.38 mmol g_{cat}^{-1} h^{-1}, exceeding 6.5 times that of the Ir_1/*d*-aUiO particles. Moreover, following similar optimization strategy, the Pd_1/*d*-aUiO membranes can convert humid O_2 to H_2O_2 with an exceptional activity of 10.4 mmol g_{cat}^{-1} h^{-1} under visible light, verifying the wide applicability of our catalyst and reaction interface designs.

RESULTS AND DISCUSSION

Catalyst synthesis. We screened a series of photosensitizers, including MOFs, inorganic semiconductors and coordination complex, as the hosts of metal SA active centers and the building blocks of our artificial photosynthesis membranes. Among these candidates, NH_2-UiO-66 (aUiO), a kind of representative MOF materials[21], represented a promising candidate with unique advantages such as high photoactivity, porosity, specific surface area, and water stability[21,22]. Especially, the versatile chemical tunability of such MOF materials allowed us to modify their chemical structures and light harvesting capabilities at the molecular level for anchoring and sensitizing external metal species with rationally designed catalytic properties[23,24]. Typically, monodispersed aUiO particles were prepared by solution method with the ligands (2-aminoterephthalic acid) partially replaced by acetates (Figure S1). These acetates were removed afterwards by activating the as-obtained aUiO particles under elevated temperature in a vacuum oven to obtain defect-rich *d*-aUiO with missing linkers and abundant defects on the edges of the $Zr_6O_4(OH)_4(\text{-}CO_2)_{12\text{-}x}$ octahedral secondary building units (SBUs, where *x* represents number of missing linkers per SBU)[25] (Figure S2). Compared with the pristine defect-deficient aUiO particles, such defects provided abundant anchoring sites to bond the subsequently introduced metal (e.g. Ir and Pd) species to obtain our SA/MOF particles and membranes (Figures S3–S11).

Selected metal single-atoms (SAs) (e.g. Ir and Pd) were then incorporated into the activated *d*-aUiO particles by impregnation and annealing treatments (see Methods). For instance, Ir SAs (1.4 wt.%) could be evenly dispersed in *d*-aUiO matrix to form Ir_1/*d*-aUiO particles, as revealed by the scanning electron microscopy (SEM) image (Figure 1c), high-angle annular dark-field scanning TEM (HAADF-STEM) image and corresponding energy-dispersive X-ray spectroscopy (EDS) maps (Figure 1d), as well as aberration-corrected HAADF-STEM (AC-HAADF-STEM) images (Figures 1e and S4). Extended X-ray absorption fine structure (EXAFS) analysis exhibited the existence of Ir–O bonds with the average coordination number of 3.8 and the absence of Ir–Ir bonding (Figure S5), further verifying the single-atomic dispersion of Ir species in the Ir_1/*d*-aUiO particles. Lowering the Ir loading to 0.7 wt.% resulted in sparser dispersion of Ir SAs in Ir_1/*d*-aUiO (Figures S6 and S7), while increasing the loading of Ir to 2.7 wt.% led to the formation of *d*-aUiO containing both Ir SAs and small clusters (Ir_x/*d*-aUiO, Figures S8 and S9). Similarly, Pd (0.8 wt.%) could also be atomically dispersed in *d*-aUiO to form Pd_1/*d*-aUiO, as confirmed by AC-HAADF-STEM and EXAFS results (Figures 1f, S10 and S11).

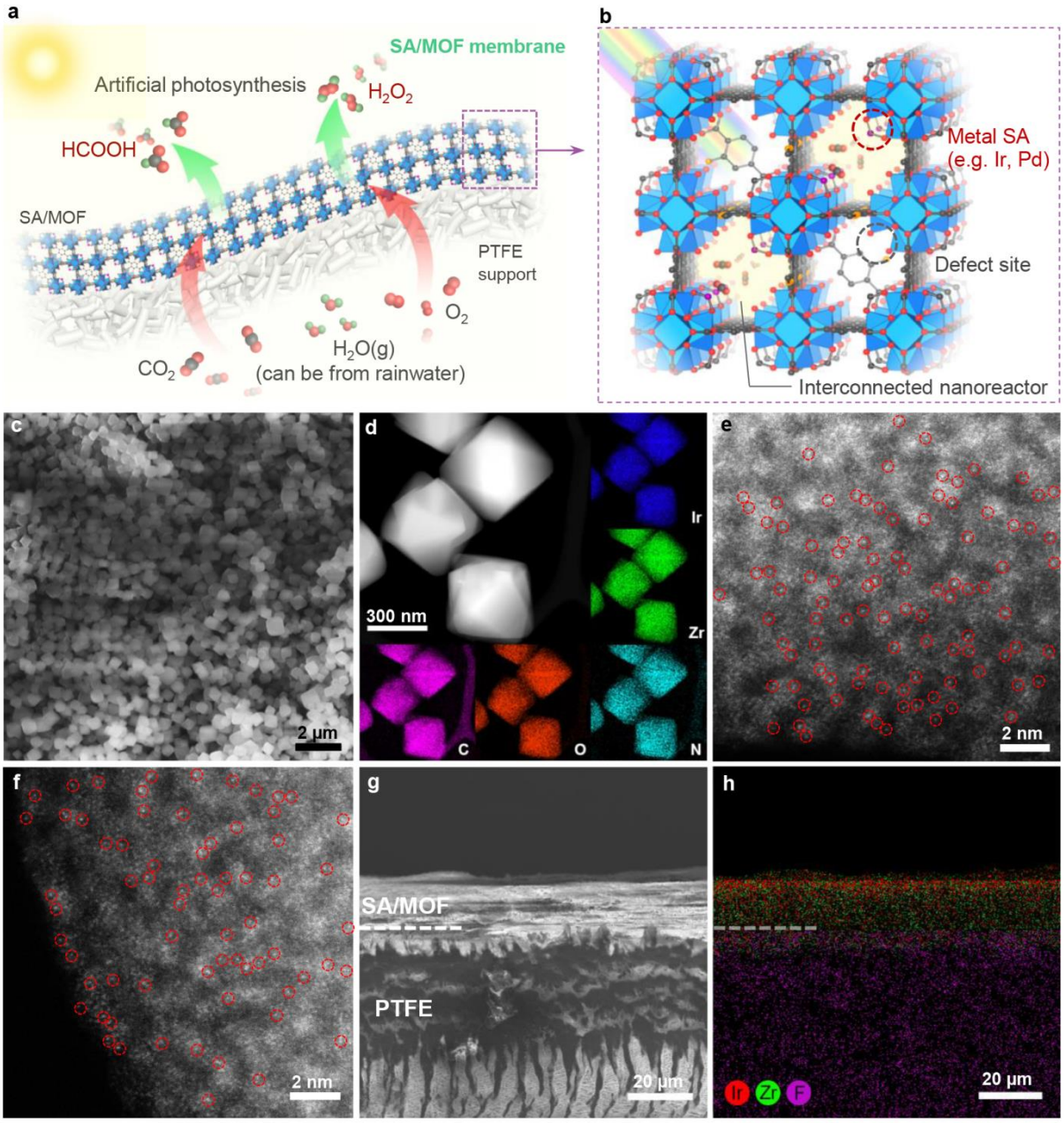

Figure 1. Schematic illustration and structural characterization of the SA/MOF membranes. (**a**) Humidified gases (e.g. CO_2, O_2) can be fed through the breathable MOF/PTFE membranes and photocatalytically reduced to value-added chemicals (e.g. HCOOH and H_2O_2) under visible light irradiation and ambient conditions. (**b**) With controllable defect-engineering, specific metal SAs (e.g. Ir and Pd) can be precisely anchored on the edges of the $Zr_6O_4(OH)_4(\text{-}CO_2)_{12\text{-}x}$ octahedral to act as programable catalytic centers for catalyzing different reactions, such as photocatalytic CO_2-to-HCOOH and O_2-to-H_2O_2 conversion. The open and interconnected MOF pores serve as the nanoreactors facilitating the diffusion and conversion of gas reactants. (**c**) SEM image for Ir_1/*d*-aUiO particles. (**d**) HAADF-STEM image and corresponding EDS maps for Ir_1/*d*-aUiO particles. (**e**, **f**) AC-HAADF-STEM images for (e) Ir_1/*d*-aUiO and (f) Pd_1/*d*-UiO, indicating the atomic dispersion of metal species in *d*-aUiO matrixes. (**g**, **h**) SEM image (g) and corresponding EDS mapping (h) for the cross section of Ir_1/*d*-aUiO/PTFE membranes.

These SA/*d*-aUiO particles were then deposited onto commercially available porous polytetrafluoroethylene (PTFE) films in a layer-by-layer manner to fabricate flexible and breathable membranes through facile filtration protocols (Figures 1g,h and S12–S16). The hierarchical channels of the PTFE films (Figure 1g) and the interconnected pores of the SA/*d*-aUiO particles naturally resembled the stomata of green leaves, facilitating the direct diffusion of gas molecules and the collision of them onto the open metal SA catalytic centers within the pores and channels of MOFs.

Photocatalytic CO_2RR. We then performed photocatalytic CO_2 reduction reaction (CO_2RR) at traditional three-phase (with Ir_1/*d*-aUiO particles) and our re-designed reaction interfaces (with Ir_1/*d*-aUiO membranes) to demonstrate the advantages of single-atomic catalytic centers and high-throughput gas-solid reaction interfaces. As revealed by ultraviolet-visible absorption spectra (Figure 2a), creating missing linkers and coordination defects on the Zr–O nodes dramatically enhanced the visible light absorption efficiency of aUiO particles[26], shifting their absorption band edge up to 600 nm in the visible region. Compared with the pristine defect-deficient aUiO and other typical semiconductor photocatalytic hosts, such as titanium dioxide (TiO_2) and carbon nitride (C_3N_4), *d*-aUiO exhibited much higher photon-to-electron conversion efficiency under visible light (> 420 nm) irradiation (Figures 2b, S17 and S18). The photogenerated electrons could be then effectively captured by active centers such as metal SAs and nanoparticles (NPs) (Figure S19).

To investigate the intrinsic activity and catalytic mechanism of our catalysts, we first monitored the CO_2RR on powder photocatalysts in the conventional particle-in-solution (PiS) mode with gas-liquid-solid reaction interfaces (Figure S20). As shown in Figure 2c, bare *d*-aUiO showed no observable CO_2RR activity. Decorating *d*-aUiO with iridium species triggered the selective and efficient photoreduction of CO_2 to formic acid. Especially, Ir SAs showed much higher formic acid activity and selectivity than Ir clusters and nanoparticles (Figure 2c,d). The 0.7 wt.% Ir_1/*d*-aUiO particles exhibited a HCOOH generation rate of 0.24 mmol g_{cat}^{-1} h^{-1} with a high selectivity of 96.3%. Increasing the Ir SAs loading to 1.4 wt.% elevated the HCOOH activity to 0.51 mmol g_{cat}^{-1} h^{-1} with the a near-unity selectivity (Figures S21 and S22), exceeding that of previously reported photocatalysts under similar conditions (Table S1). In sharp contrast, iridium clusters and nanoparticles (i.e. Ir_x/*d*-aUiO and IrNPs/*d*-aUiO, respectively) suffered from strong hydrogen evolution reaction (HER) competition and showed inferior CO_2RR performance (Figures 2d and S23), suggesting that the chemical structures of Ir species and their interactions with the *d*-aUiO hosts played a critical role in the selective photoreduction of CO_2 to HCOOH. Compared with Ir clusters and nanoparticles, the Ir SAs were more electron-deficient as revealed by X-ray absorption near-edge structure (XANES) and X-ray photoelectron spectroscopy (XPS) analysis (Figures 2e and S24). Such differences in electronic structures may thereby result in their different catalytic reactivity. As shown in Figure 2f, the Ir_1/*d*-aUiO catalyst showed much lower apparent activation energy (E_{app}) for HCOOH evolution (9.8 kJ mol^{-1}) than Ir_x/*d*-aUiO (25.1 kJ mol^{-1}) and IrNPs/*d*-aUiO (55.6 kJ mol^{-1}), suggesting the much faster CO_2RR kinetics on Ir_1/*d*-aUiO under similar conditions. Thus, the strong metal-substrate interactions could substantially modulate the electronic structures of Ir species, and the highly electron-deficient Ir SAs presented the best CO_2RR activity and selectivity targeting HCOOH production.

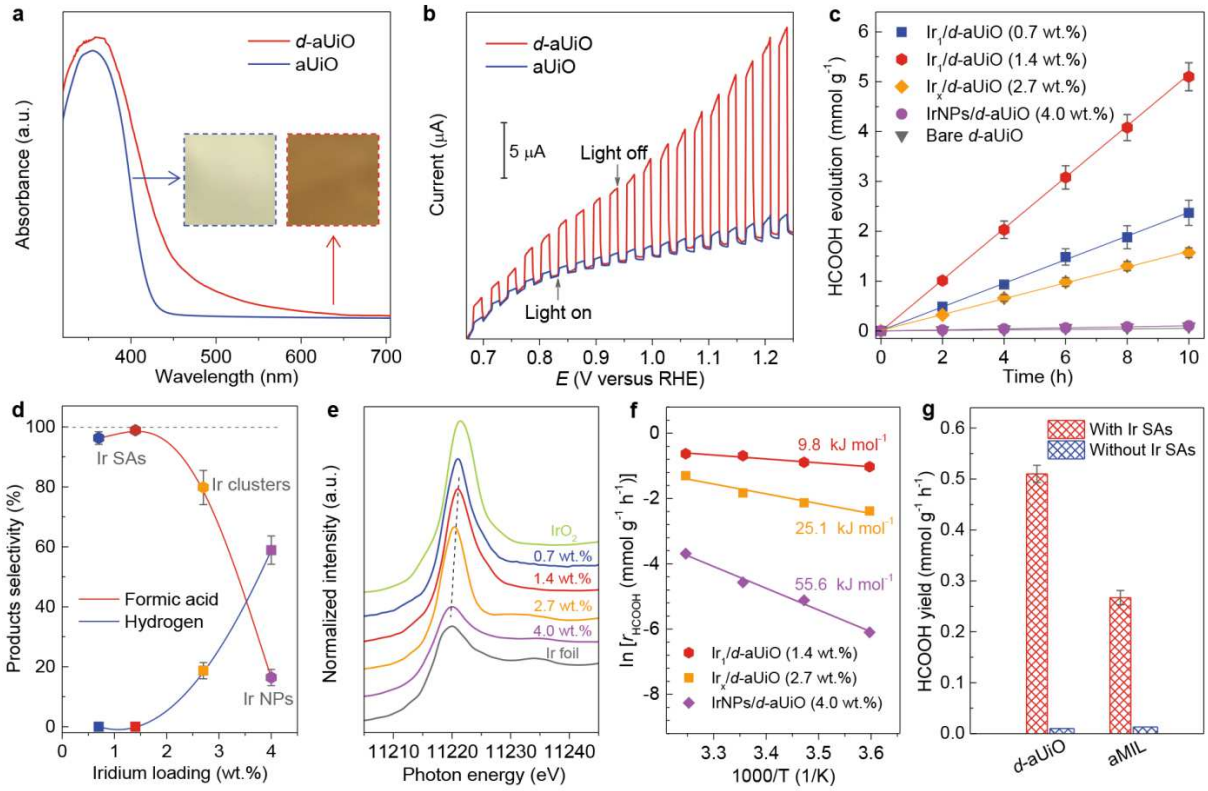

Figure 2. Photocatalytic CO_2RR on SA/MOF powder catalysts. (**a, b**) The enhancing of light harvesting and conversion efficiency for *d*-aUiO through defects engineering. UV-vis diffusive reflectance spectra (a) and photocurrent-potential curves (b) for *d*-aUiO and a-UiO samples, respectively. Inset in (a): Digital photograph showing the colour of aUiO and *d*-aUiO samples. (**c**) Time course of HCOOH evolution on *d*-aUiO, Ir_1/*d*-aUiO, Ir_x/*d*-aUiO and IrNPs/*d*-aUiO catalysts. (**d**) HCOOH and H_2 selectivity as a function of Ir loadings in Ir/*d*-aUiO catalysts. (**e**) Ir L-edge XANES spectra of Ir/*d*-aUiO catalysts with different Ir loadings. Ir foil and IrO_2 were used as standards. The first maximum of the XANES curves after the absorption edge (dashed line) shows gradual positive movement with decreasing Ir loading, suggesting the metallicity of the Ir species was gradual decreased. (**f**) Apparent activation energy (E_{app}) of various catalysts for HCOOH generation. (**g**) HCOOH yields on *d*-aUiO and aMIL catalysts with and without Ir SAs modification. All the photocatalytic reactions were performed under visible light (> 420 nm) irradiation and using isopropanol (20 v/v% in water) as sacrificial agents. Error bars were calculated by carrying out three parallel catalysis reactions.

The reaction route for CO_2RR on the Ir_1/*d*-aUiO catalyst was further studied by isotope-labeled mass spectroscopy (MS) and *in situ* Fourier-transform infrared spectroscopy (FTIR). As revealed by the electrospray ionization-mass spectrometry (ESI-MS) (Figure S25), $H^{13}COO^-$ was the only product when $^{13}CO_2$ was used as feed gas, confirming that the formates were generated from photocatalytic CO_2RR exclusively. Additionally, as shown in Figure S26, FTIR peaks (at 1497 and 1433 cm^{-1}) of the surface carbonic acid species[27,28], the intermediate species for formic acid evolution[27], were immediately observed when humidified CO_2 was fed into the reactors containing Ir_1/*d*-aUiO or *d*-aUiO catalysts in dark, indicating the adsorption of CO_2 by the hydroxyls on the Zr–O nodes of *d*-aUiO[29,30]. The reactors were then purged with Ar to remove the excess CO_2. Under visible light irradiation, new infrared peaks (at 2920, 2850 and 1576 cm^{-1}) were observed on the Ir_1/*d*-aUiO catalyst (Figure S27a), suggesting the formation of HCOO* species upon irradiation[31–33]. To the contrary, no significant HCOO* peaks could be found in the FTIR spectra for the bare *d*-aUiO catalyst (Figure S27b). Therefore, a plausible reaction route for photocatalytic CO_2RR on Ir_1/*d*-aUiO would be that the CO_2 molecules were first adsorbed by the *d*-aUiO to form surface carbonic acid species and then hydrogenated on the Ir_1 catalytic centers with photogenerated

electrons provided by the *d*-aUiO matrix and protons (from water) to form HCOOH[34,35]. Interestingly, similar photocatalytic CO_2RR route for HCOOH production can be also enabled on other Ir/MOF catalysts. For instance, NH_2-MIL-125(Ti)[36] (aMIL) decorated by Ir SAs (Ir_1/aMIL, Figure S28) showed significantly higher CO_2RR activity than the pristine aMIL components. Under visible light irradiation, the HCOOH evolution rates were 0.27 and 0.013 mmol g_{cat}^{-1} h^{-1}, with the E_{app} of 20.1 and 58.7 kJ mol^{-1}on Ir_1/aMIL and bare aMIL, respectively (Figures 2g and S29). Therefore, the synergy between the MOF matrix and the Ir SA active centers contributes to CO_2RR for HCOOH evolution with high activity and selectivity.

Reaction interface design. Along with the catalytic center optimization, fabricating porous SA/MOF membranes allows us to build novel gas-solid reaction interfaces that can break the mass transfer limitation for gas reactants to further promote CO_2RR. Compared with the PiS mode in which the local concentration of CO_2 in the vicinity of catalyst surfaces is restricted by their low solubility and sluggish diffusion in aqueous solutions (Figure 3a), the updated gas-membrane-gas (GMG) (Figures 3b, S30 and S31) configuration can significantly decrease the diffusional lengths and resistance for gas reactants. As a result, the molecular ratio of CO_2/H_2O in the vicinity of each catalytic centers can be increased by 4 orders of magnitude from 1/1600 (saturated CO_2 solutions, PiS) to ~30/1 (CO_2 gas with saturated H_2O steam, GMG)[17]. The increase of local CO_2 concentration and the reverse of CO_2/H_2O ratio in the SA/MOF membranes would thus dramatically enhance the CO_2RR activity in a wide range of CO_2 flow rates (Figure 3d). For instance, with the CO_2 flow rate fixed at 120 standard cubic centimeters per minute (sccm), the Ir_1/*d*-aUiO membrane exhibited an HCOOH yield of 3.38 mmol g_{cat}^{-1} h^{-1} in the GMG mode, exceeding more than 6.5 times that showed by Ir_1/*d*-aUiO particles in the conventional PiS mode.

The advantages of the SA/MOF membranes and the GMG reaction interfaces were further demonstrated by measuring the photocatalysis performance at different CO_2 availability. As shown in Figure 3e, in the PiS mode, the HCOOH evolution rate increased gradually with the volume fractions of CO_2 concentrations in the mixture of CO_2 and Ar [i.e. CO_2/(CO_2 + Ar), v/v%]. To the contrary, the HCOOH yield increased rapidly and reached to the plateau at low CO_2 concentrations (< 40 v/v%) in the GMG mode. Notably, in the relatively low CO_2 concentration region (< 60 v/v%), the GMG configuration exhibited an order of magnitude higher HCOOH generation rate compared with the conventional PiS mode. These results further confirm that the Ir_1/*d*-aUiO membranes can enable efficient gas mass transfer, thereby enrich CO_2 with relatively low initial concentrations, and turn them into HCOOH with much higher efficiency than the powder catalysts dispersed in aqueous solutions. In addition, the photocatalytic activity and selectivity of the Ir_1/*d*-aUiO membranes remained stable over the long-term operation of 100 hours (Figure 3f). With the near-unity selectivity, the formic acid productivity was as high as 3.38 mmol g_{cat}^{-1} h^{-1}, which is more than 6.5 times higher than previously reported best values (Table S1).

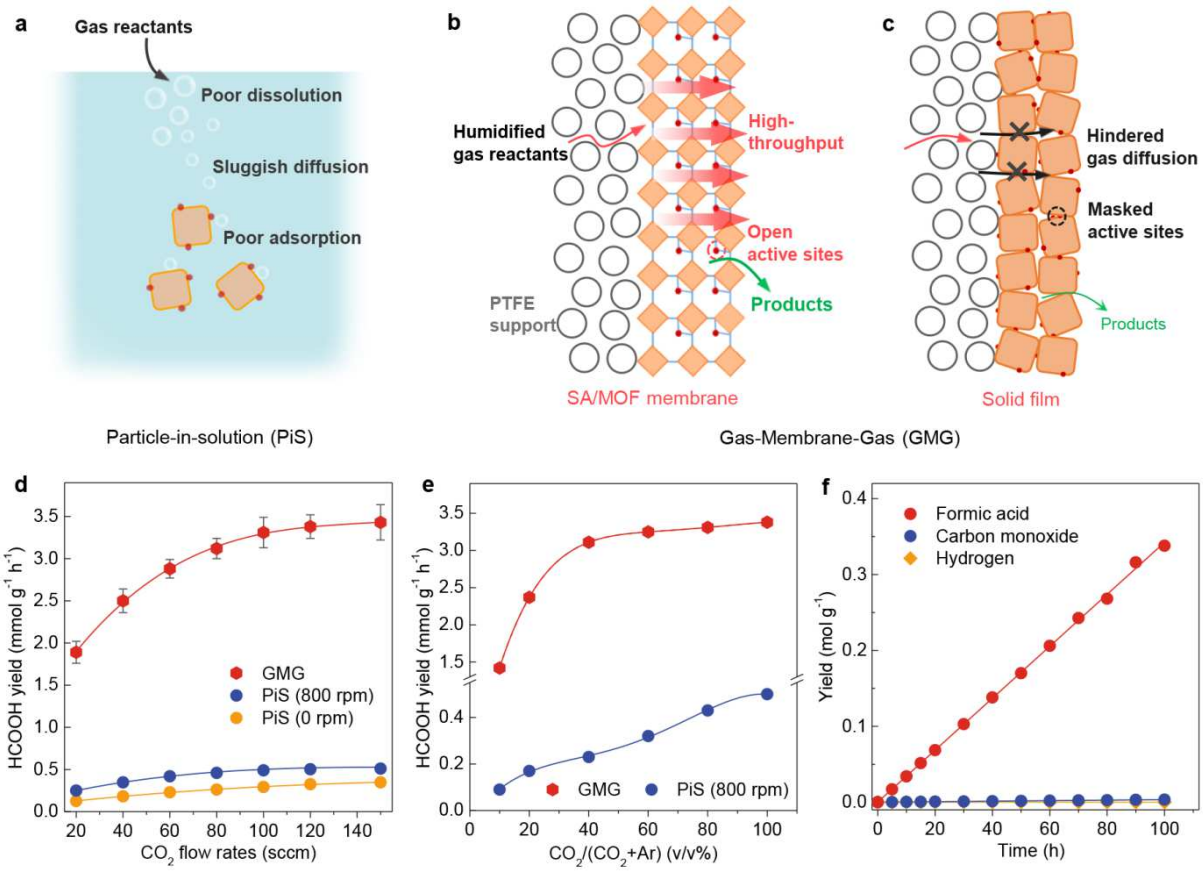

Figure 3. Photocatalytic CO_2RR on SA/MOF membranes. (**a**) In the particle-in-solution (PiS) mode, gas-phase CO_2 was fed into the aqueous photocatalyst dispersion and then reduced on the water flooded surfaces of catalysts. (**b**) In the gas-membrane-gas (GMG) mode, humidified CO_2 gas was fed through the SA/MOF membrane, where water vapor was carried by the CO_2 stream. (**c**) Schematic illustration for the solid films fabricated by non-porous semiconductor particles. (**d**) HCOOH yields on Ir_1/*d*-aUiO particles (PiS) and membrane (GMG) under different CO_2 flow rates, respectively. (**e**) HCOOH yields on Ir_1/*d*-aUiO particles (PiS) and membrane (GMG) under different CO_2 concentration (in Ar mixtures), respectively. (**f**) Time course of HCOOH, CO and H_2 evolution on Ir_1/*d*-aUiO membrane (GMG). All the photocatalytic reactions were performed under visible light (> 420 nm). The CO_2 flow rates in (e) and (f) were fixed at 120 sccm. Error bars represent the standard deviation for three independent catalysis tests.

Further control experiments also suggested the vital role of the highly porous MOF matrix in constructing such high-throughput gas-solid catalytic interfaces. The porous Ir_1/*d*-aUiO and Ir_1/aMIL membranes exhibited a 5.6- and 4.8-fold enhancement in CO_2RR activity as compared with their powder counterparts, respectively; however, the solid films composed of non-porous inorganic particles (e.g. Ir/TiO_2, Ir/ZnO) showed a much lower activity enhancement (~40%) (Figures S32–S36). These significant differences in enhancement factors for CO_2RR on MOF membranes and solid films may arise from their markedly different mass transfer and photoelectron deliver efficiencies (Figure 3b,c). Thanks to the ultrahigh porosity and open pore structure of MOF matrixes, the diffusion of CO_2/H_2O molecules from gas phase to the highly dispersed active centers would be efficient in high throughput (Figure S37). The delivery of photoelectrons from the local ligands to the active sites also not be hindered by stacking SA/MOF particles. However, the aggregation of solid semiconductor particles would form a solid film that would retard the efficient diffusion of gas molecules to the surface active sites (Figures 3c and S37), further suppressing the photocatalytic reduction of CO_2 on such solid films.

The use of water vapor instead of aqueous solutions as proton sources brought additional advantages for CO_2RR. As shown in Figure S38, in the PiS mode, the HCOOH evolution rate significantly declined when tap water or rainwater (both collected on the BIT campus in Beijing) was used as proton sources instead of the ultrapure DI water. The decrease in catalyst activity would be possibly caused by the impurities in tap water or rainwater (e.g. Cl^-, ClO^- and other ions), which may poison the active centers. However, using the naturally purified water vapor as proton sources could effectively avoid the poisoning of catalyst from such impurities and ensure the HCOOH yield despite the types of water sources. Therefore, our SA/MOF membranes and GMG interface designs exhibited great potential in fixing relatively low-concentration CO_2 to HCOOH with high selectivity and activity, using naturally available water as proton sources and visible light as energy supplies.

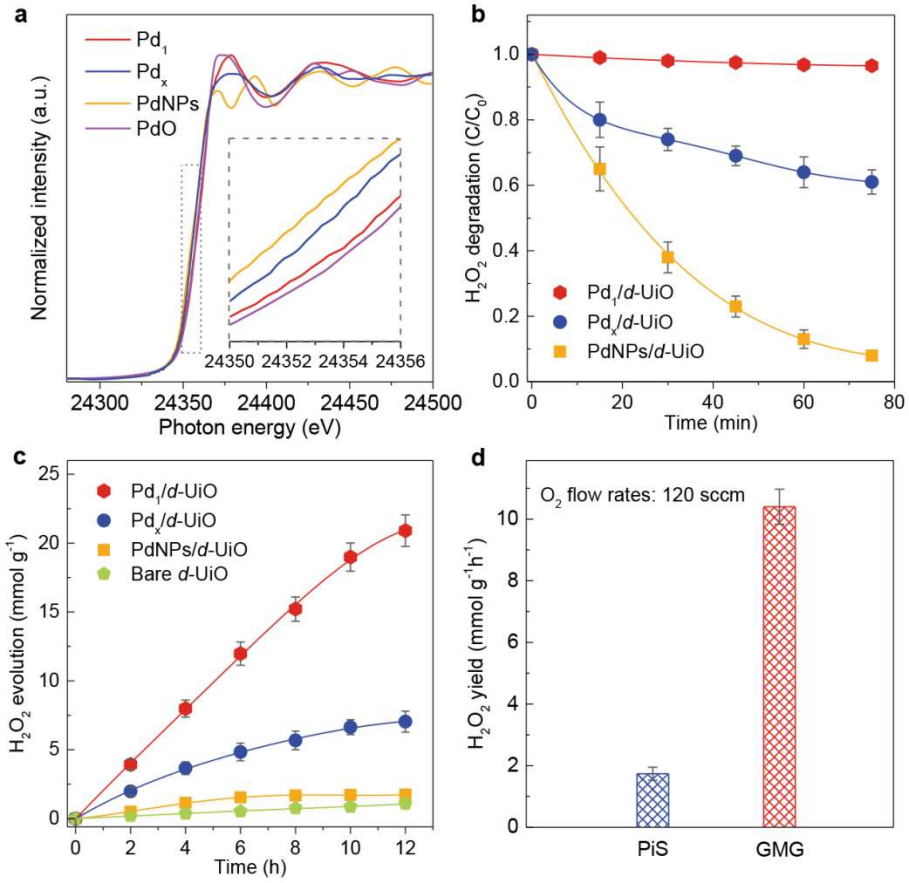

Figure 4. Photocatalytic O_2 reduction (ORR) on Pd modified MOF powders and membrane. (**a**) Pd K-edge XANES spectra of PdNPs, Pd_x and Pd_1 decorated *d*-aUiO catalysts. PdO was used as standard. (**b**) Time course of H_2O_2 decomposition on PdNPs, Pd_x and Pd_1 decorated *d*-aUiO catalysts. (**c**) Time course of H_2O_2 generation on pristine *d*-aUiO and PdNPs, Pd_x and Pd_1 decorated *d*-aUiO catalysts. (**d**) H_2O_2 yields on Ir_1/*d*-aUiO particles (PiS) and membranes (GMG), respectively. All the photocatalytic reactions were performed under visible light (> 420 nm) irradiation and using isopropanol (20 v/v% in water) as sacrificial agents. The O_2 flow rates were fixed at 120 sccm. Error bars represent the standard deviation for three independent catalysis tests.

Photocatalytic oxygen reduction reaction. Notably, the wide applicability of our catalyst and reaction interface design strategy can be further applied to the photoreduction of O_2 to H_2O_2 (Figure 4). Like Ir/*d*-aUiO, the strong metal-substrate interactions could also modulate the electronic structures of Pd species (e.g. Pd SAs, clusters, and nanoparticles) supported

by *d*-aUiO matrix (Figures 4a, S39 and S40). As compared with the Pd clusters and nanoparticles, the electron-deficient Pd_1 sites could not only significantly promote H_2O_2 generation (Figure S41) but also effective suppress H_2O_2 decomposition[37] (Figure 4b). As a result, in the PiS mode, Pd_1/*d*-aUiO particles exhibited an H_2O_2 yield (1.74 mmol g_{cat}^{-1}) that was more than 3 and 12 times that of Pd_x/*d*-aUiO (0.58 mmol g_{cat}^{-1}) and PdNPs/*d*-aUiO (0.14 mmol g_{cat}^{-1}), respectively (Figure 4c). Further enhancement in H_2O_2 generation activity was realized by reacting humidified O_2 gas flow on Pd_1/*d*-aUiO membrane in the GMG mode, showing an unprecedented H_2O_2 evolution rate (10.4 mmol g_{cat}^{-1} h^{-1}) that was more than 4.9-fold higher than that observed in the PiS mode (Figure 4d and Table S2). That is, the breathable MOF (e.g. *d*-aUiO, aMIL) membranes can serve as a versatile array of photosensitizer and nanoreactor to host different metal SAs (e.g. Ir, Pd) for the selective photocatalytic reduction of specific gases into chemical fuels under visible light and mild conditions.

CONCLUSIONS

The highly porous SA/MOF membranes decorated with single-atomic reaction centers, assembling numerous regularly arranged and interconnected photocatalytic nanoreactors, bridge the best of homogeneous and heterogeneous catalysis. On one hand, like molecular catalysts, the explicit structures for the highly dispersed photocatalyst modules (ligand–node–SA) allow us to modify their light harvesting, electron delivery and catalytic conversion properties with atomic precision. On the other hand, the porous but rigid MOF crystals hold all the nanoreactors together via stable coordination bonds with interconnected pores, ensuring the high stability, dispersity, and accessibility of the atomically dispersed catalytic centers. Especially, starting with humidified gas instead of gas solutions, the novel GMG reaction interfaces not only facilitate the diffusion of gas molecules but also eliminate the competitive adsorption of liquid water, which is inevitable in conventional three-phase photocatalytic gas reduction reactions. The substantial increase in local concentration and molar ratio of gas reactants in the vicinity of each catalytic center thereby promote the activity and selectivity of photocatalytic reduction of gas molecules significantly.

In practice, our SA/MOF membranes can directly reduce CO_2 and O_2 into value-added and ready-to-use chemical fuels (i.e. HCOOH and H_2O_2). With specifically designed catalytic centers, the major components of air (CO_2, O_2 and even N_2) could be fixed via sustainable photocatalytic reactions with water vapor as proton donors under mild conditions to convert and store the intermittent solar energy. The facile preparation of SA/MOF membranes facilitates the scale-up of such photocatalysis devices and the minimized usage of water vapor saves the cost of freshwater in arid regions with rich solar powers. Our work provides a general and programmable strategy bridging photocatalysis center and reaction interface designs to solve the complexity for mass transfer and catalytic conversion in three-phase photocatalytic reactions. The powerful toolbox in single-atom and MOF chemistry endows us with almost infinite possibilities to engineer the chemical structures of SA/MOF membranes. Such design may find wider applicability in more substantial heterogeneous reactions.

References:

1. Larkum, A. W. Limitations and prospects of natural photosynthesis for bioenergy production. *Curr. Opin. Biotech*. **21**, 271–276 (2010).
2. Atsumi, S., Higashide, W. & Liao, J. C. Direct photosynthetic recycling of carbon dioxide to isobutyraldehyde. *Nat. Biotechnol.* **27,** 1177–1180 (2009).
3. Sakimoto, K. K., Wong, A. B. & Yang, P. D. Self-photosensitization of nonphotosynthetic bacteria for solar-to-chemical production. *Science* **351**, 74–77 (2016).
4. Ran, J. R., Jaroniec, M. & Qiao, S. Z. Cocatalysts in semiconductor-based photocatalytic CO_2 reduction: achievements, challenges, and opportunities. *Adv. Mater*. **30**, 1704649 (2018).
5. Kornienko, N., Zhang, J. Z., Sakimoto, K. K., Yang, P. D. & Reisner, E. Interfacing nature's catalytic machinery with synthetic materials for semi-artificial photosynthesis. *Nat. Nanotechnol*. **13**, 890–899 (2018).
6. Li, A., Cao, Q., Zhou, G. Y., Schmidt, B. V. K. J., Zhu, W. J., Yuan, X. T., Huo, H. L., Gong, J. L. & Antonietti, M. Three-phase photocatalysis for the enhanced selectivity and activity of CO_2 reduction on a hydrophobic surface. *Angew. Chem. Int. Ed.* **58**, 14549–14555 (2019).
7. Li, X. D., Sun, Y. F., Xu, J. Q., Shao, Y. J., Wu, J., Xu, X. L., Pan, Y., Ju, H. X., Zhu, J. F. & Xie, Y. Selective visible-light-driven photocatalytic CO_2 reduction to CH_4 mediated by atomically thin $CuIn_5S_8$ layers. *Nat. Energy* **4**, 690–699 (2019).
8. Deng, J., Su, Y. D., Liu, D., Yang, P. D., Liu, B. & Liu, C. Nanowire photoelectrochemistry. *Chem. Rev*. **119**, 9221–9259 (2019).
9. Lin, R. X., Xiao, K., Qin, Z. Y., Han, Q. L., Zhang, C. F., Wei, M. Y., Saidaminov, M., Gao, Y., Xu, J., Xiao, M., Li, A. D., Zhu, J., Sargent, E. H. & Tan, H. R. Monolithic all-perovskite tandem solar cells with 24.8% efficiency exploiting comproportionation to suppress Sn(ii) oxidation in precursor ink. *Nat. Energy* **4**, 864–873 (2019).
10. Cestellos-Blanco, S., Zhang, H., Kim, J. M., Shen, Y. X. & Yang. P. D. Photosynthetic semiconductor biohybrids for solar-driven biocatalysis. *Nat. Catal*. **3**, 245–255 (2020).
11. Gao, C., Wang, J., Xu, H. X. & Xiong, Y. J. Coordination chemistry in the design of heterogeneous photocatalysts. *Chem Soc Rev*. **46**, 2799–2823 (2017).
12. Rao, H., Schmidt, L. C., Bonin, J. & Robert, M. Visible-light-driven methane formation from CO_2 with a molecular iron catalyst. *Nature* **548**, 74–77 (2017).
13. Ma, B., Chen, G., Fave, C., Chen, L. J., Kuriki, R., Maeda, K., Ishitani, O., Lau, T. C., Bonin. J. & Robert, M. Efficient visible-light-driven CO_2 reduction by a cobalt molecular catalyst covalently linked to mesoporous carbon nitride. *J. Am. Chem. Soc*. **142**, 6188–6195 (2020).
14. Hu, Y. G., Zhan, F., Wang, Q., Sun, Y. J., Yu. C., Zhao, X., Wang, H., Long, R., Zhang, G. Z., Gao, C., Zhang, W. K., Jiang, J., Tao, Y. & Xiong, Y. J. Tracking mechanistic pathway of photocatalytic CO_2 reaction at Ni sites using operando, time-resolved spectroscopy. *J. Am. Chem. Soc*. **142**, 5618–5626 (2020).
15. Liu, P. X., Zhao, Y., Qin, R.X., Mo, S. G., Chen, G. X., Gu, L., Chevrier, D. M., Zhang, P., Guo, Q., Zang, D. D., Wu, B. H., Fu, G. & Zheng, N. F. Photochemical route for synthesizing atomically dispersed palladium catalysts. *Science* **352**, 797–801 (2016).
16. Bhosale, S. S., Kharade, A. K., Jokar, E., Fathi, A., Chang, S. M. & Diau, E. W. Mechanism of photocatalytic CO_2 reduction by bismuth-based perovskite nanocrystals at the gas-solid interface. *J. Am. Chem. Soc*. **141**, 20434–20442 (2019).
17. Li, J., Chen, G. X., Zhu, Y. Y., Liang, Z., Pei, A., Wu, C. L., Wang, H. X., Lee, H. R., Liu, K., Chu, S. & Cui, Y.

Efficient electrocatalytic CO_2 reduction on a three-phase interface. *Nat. Catal*. **1**, 592–600 (2018).

18. Garcia de Arquer, F. P., Dinh, C. T., Ozden, A., Wicks, J., McCallum, C., Kirmani, A. R., Nam, D. H., Gabardo, C., Seifitokaldani, A., Wang, X., Li, Y. C., Li, F., Edwards, J., Richter, L. J., Thorpe, S. J., Sinton, D. & Sargent, E. H. CO_2 electrolysis to multicarbon products at activities greater than 1 A cm^{-2}. *Science* **367**, 661–666 (2020).
19. Goyal, A., Marcandalli, G., Mints, V. A. & Koper, M. T. M. Competition between CO_2 reduction and hydrogen evolution on a gold electrode under well-defined mass transport conditions. *J. Am. Chem. Soc*. **142**, 4154–4161 (2020).
20. Wu, J., Li, X. D., Shi, W., Ling, P. Q., Sun, Y. F., Jiao, X. C., Gao, S., Liang, L., Xu, J. Q., Yan, W. S., Wang, C. M. & Xie, Y. Efficient visible-light-driven CO_2 reduction mediated by defect-engineered BiOBr atomic layers. *Angew. Chem. Int. Ed.* **57**, 8719–8723 (2018).
21. Cavka, J. H. & Lillerud, K. P. A new zirconium inorganic building brick forming metal organic frameworks with exceptional stability. *J. Am. Chem. Soc*. **130**, 13850–13851 (2008).
22. Sun, D. R. & Li, Z. H. Studies on Photocatalytic CO_2 Reduction over NH_2-UiO-66(Zr) and its derivatives: towards a better understanding of photocatalysis on metal-organic frameworks. *Chem. Eur. J.* **19**, 14279–14285 (2013).
23. Furukawa, H., Cordova, K. E., O'Keeffe, M. & Yaghi, O. M. The chemistry and applications of metal-organic frameworks. *Science* **341**, 1230444–1230456 (2013).
24. Kalmutzki, M. J., Hanikel, N. & Yaghi, O. M. Secondary building units as the turning point in the development of the reticular chemistry of MOFs. *Sci. Adv* **4**, eaat9180 (2018).
25. Trickett, C. A., Gagnon, K. J., Lee, S., Gándara, F., Bürgi, H. B. & Yaghi, O. M. Definitive molecular level characterization of defects in UiO-66 crystals. *Angew. Chem. Int. Ed.* **54,** 11162–11167 (2015).
26. Vos, D. A., Hendrickx, K., Voort, P. V. D., Speybroeck, V. V. & Lejaeghere, K. Missing linkers: an alternative pathway to UiO-66 electronic structure engineering. *Chem Mater* **29**, 3006–3019 (2017).
27. Deng, W. Y., Zhang, L. Gong, J. L. Crucial role of surface hydroxyls on the activity and stability in electrochemical CO_2 reduction. *J. Am. Chem. Soc*. **141**, 2911–2915 (2019).
28. Mu, R., Zhao, Z. J., Dohnálek, Z. & Gong, J. L. Structural motifs of water on metal oxide surfaces. *Chem. Soc. Rev*. **46**, 1785−1806 (2017).
29. Chevreau, H. & Peterson, V. K. Concentration-dependent binding of CO_2 and CD_4 in UiO-66(Zr). *J. Phys. Chem. C*. **119**, 6980–6987 (2015).
30. Grissom, T. G.& Morris, J. R. Molecular-level insight into CO_2 adsorption on the zirconium based metal-organic framework, UiO-66: a combined spectroscopic and computational approach. *J. Phys. Chem. C*. **123**, 13731–13738 (2019).
31. Shido, T. & Iwasawa, Y. C. Regulation of reaction intermediate by reactant in the water-gas shift reaction on CeO_2 in relation to reactant-promoted mechanism. *J. Catal*. **136**, 493–503 (1992).
32. Sun, S. & Li, C. X. Photocatalytic oxidation of gaseous formaldehyde on TiO_2: an in-situ DRIFTS study. *Catal. Lett*. **137**, 239–246 (2010).
33. Graciani, J. & Rodriguez, J. A. Highly active copper-ceria and copper-ceria-titania catalysts for methanol synthesis from CO_2. *Science* **345**, 546–550 (2014).
34. Shao, X. Z., Yang, X. F. & Huang, Y. Q. Iridium single-atom catalyst performing a quasi-homogeneous hydrogenation transformation of CO_2 to formate. *Chem*. **5**, 693–705 (2019).
35. An, B., Cheng, J., Wang, C. & Lin, W. B. Molecular iridium complexes in metal-organic frameworks catalyze CO_2 hydrogenation via concerted proton and hydride transfer. *J. Am. Chem. Soc*. **139**, 17747–17750 (2017).
36. Dan-Hardi, M., Sanchez, C. & Férey, C. A new photoactive crystalline highly porous titanium(IV) dicarboxylate. *J. Am.*

Chem. Soc. **131**, 10857–10859 (2009).

37. Freakley, S. G., He, Q., Harrhy, J. H., Lu, L., Crole, D. A., Morgan, D. J., Ntainjua, E. N., Edwards, J. K., Carley, A. F., Borisevich, A. Y., Kiely, C. J. & Hutchings, G. J. Palladium-tin catalysts for the direct synthesis of H_2O_2 with high selectivity. *Science* **351**, 965–968 (2016).

Acknowledgments The authors acknowledge the Analytical and Testing Center of BIT for technical supports. A.X.Y. acknowledges the financial support by the National Natural Science Foundation of China (No. 21601015 and No. 21971012) and the Beijing Institute of Technology Research Fund Program for Young Scholars. B.W. acknowledges the National Natural Science Foundation of China (No. 61933002, 81601549, 21674012 and 21625102) and Beijing Municipal Science and Technology Project (Z181100004418001).

Author contributions A.X.Y. and B.W. designed the research. Y.C.H. and L.W.C. synthesized the catalysts, conducted the structure analysis and photocatalytic studies. Y.C.H., L.W.C., Y.G., M.S. and R.S. performed the X-ray-absorption fine-structure analysis. Q.H.Z. and L.G. performed the electron microscopy study. J.N.L and X.S. assisted with the material synthesis, characterizations, and catalysis measurements. Y.C.H. and A.X.Y. co-wrote the paper. A.X.Y. and B.W. supervised the research. All authors discussed the results and assisted during manuscript preparation.

Competing interests: Authors declare no competing interests.

Additional information

Reprints and permissions information is available at http://www.nature.com/reprints.

Correspondence and requests for materials should be addressed to A.X.Y. or R.S or B.W.

Figures

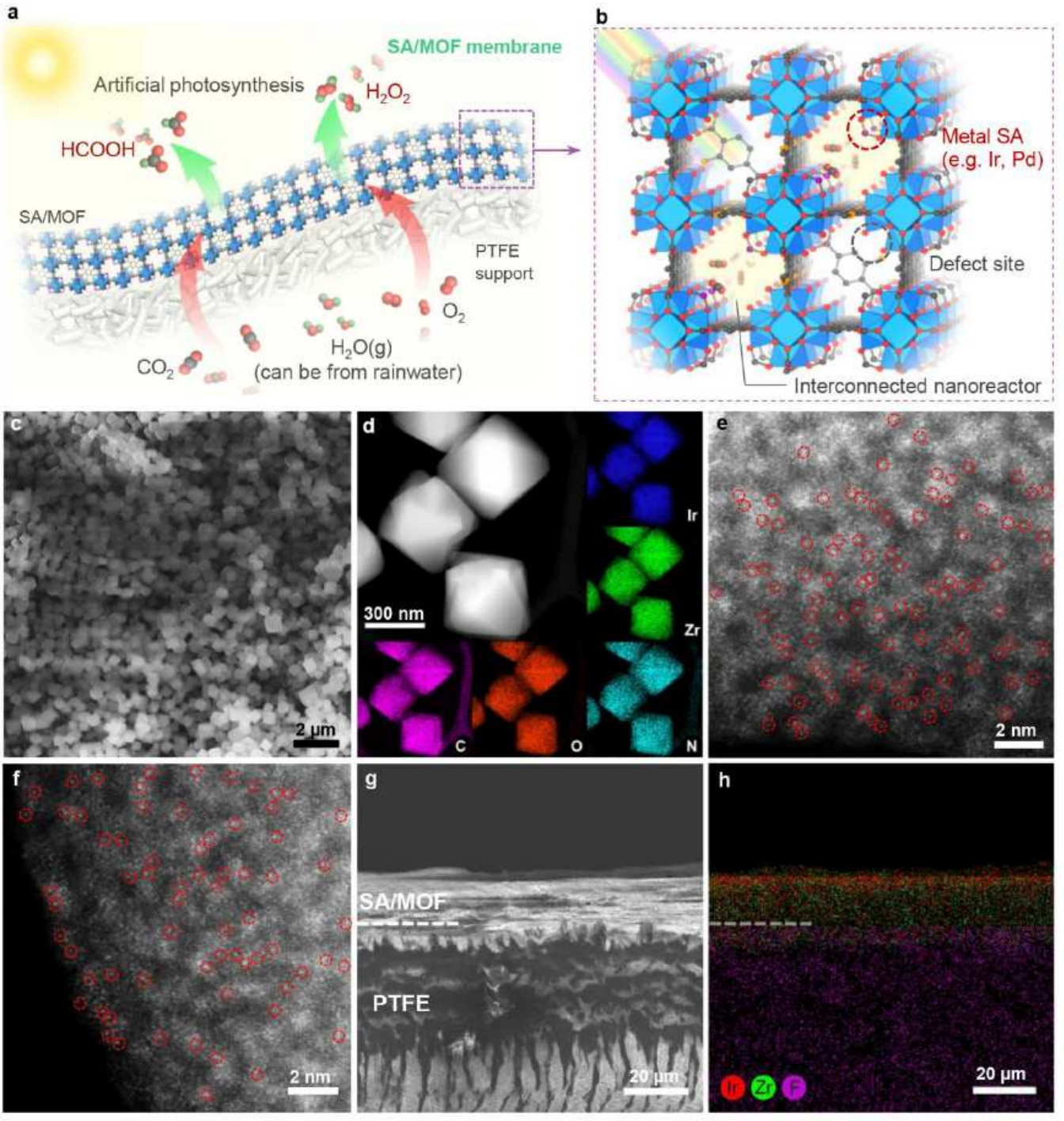

Figure 1

Schematic illustration and structural characterization of the SA/MOF membranes. (a) Humidified gases (e.g. CO2, O2) can be fed through the breathable MOF/PTFE membranes and photocatalytically reduced to value added chemicals (e.g. HCOOH and H2O2) under visible light irradiation and ambient conditions. (b) With controllable defect engineering, specific metal SAs (e.g. Ir and Pd) can be precisely anchored on the edges of the Zr6O4(OH) CO2)12-x octahedral to act as programable catalytic centers for catalyzing

different reactions, such as photocatalytic CO2 to HCOOH and O2 to H2O2 conversion. The open and interconnected MOF pores serve as the nanoreactors facilitating the diffusion and conversion of gas reactants. (c) SEM image for Ir1/d aUiO particles. (d) HAADF STEM image and corresponding EDS maps for Ir1/d-aUiO particles. (e, f) AC HAADF STEM images for (e) Ir1/d aUiO and (f) Pd1/d-UiO, indicating the atomic dispersion of metal species in d aUiO matrixes. (g, h) SEM image (g) and corresponding EDS mapping (h) for the cross section of Ir1/d aUiO/PTFE membranes.

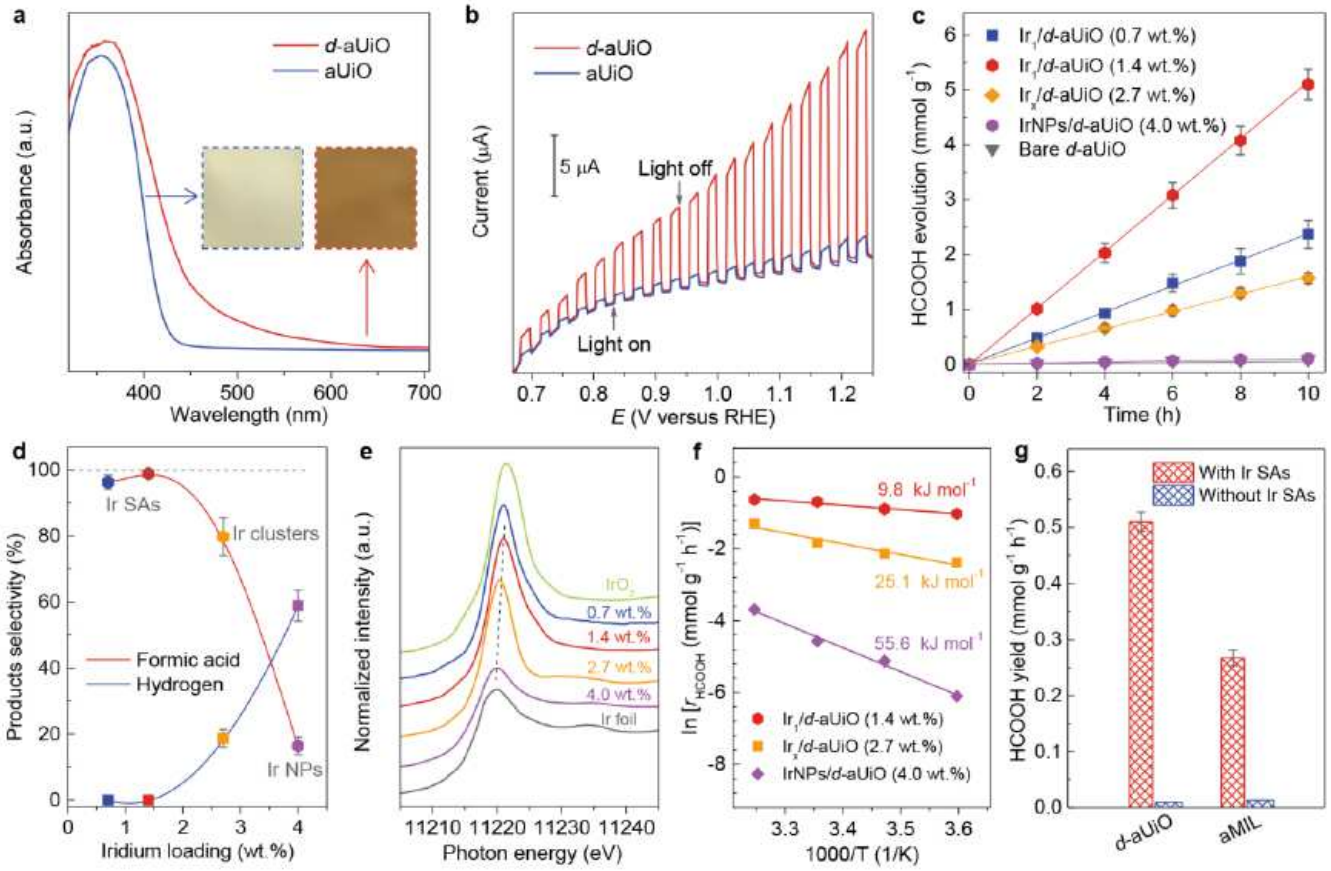

Figure 2

Photocatalytic CO2RR on SA/MOF powder catalysts. (a, b) The enhancing of light harvesting and conversion efficiency for d-aUiO through defects engineering. UV-vis diffusive reflectance spectra (a) and photocurrent-potential curves (b) for d-aUiO and a-UiO samples, respectively. Inset in (a): Digital photograph showing the colour of aUiO and d-aUiO samples. (c) Time course of HCOOH evolution on d-aUiO, Ir1/d-aUiO, Irx/d-aUiO and IrNPs/d-aUiO catalysts. (d) HCOOH and H2 selectivity as a function of Ir loadings in Ir/d-aUiO catalysts. (e) Ir L-edge XANES spectra of Ir/d-aUiO catalysts with different Ir loadings. Ir foil and IrO2 were used as standards. The first maximum of the XANES curves after the absorption edge (dashed line) shows gradual positive movement with decreasing Ir loading, suggesting the metallicity of the Ir species was gradual decreased. (f) Apparent activation energy (Eapp) of various catalysts for HCOOH generation. (g) HCOOH yields on d-aUiO and aMIL catalysts with and without Ir SAs modification. All the photocatalytic reactions were performed under visible light (> 420 nm) irradiation

and using isopropanol (20 v/v% in water) as sacrificial agents. Error bars were calculated by carrying out three parallel catalysis reactions.

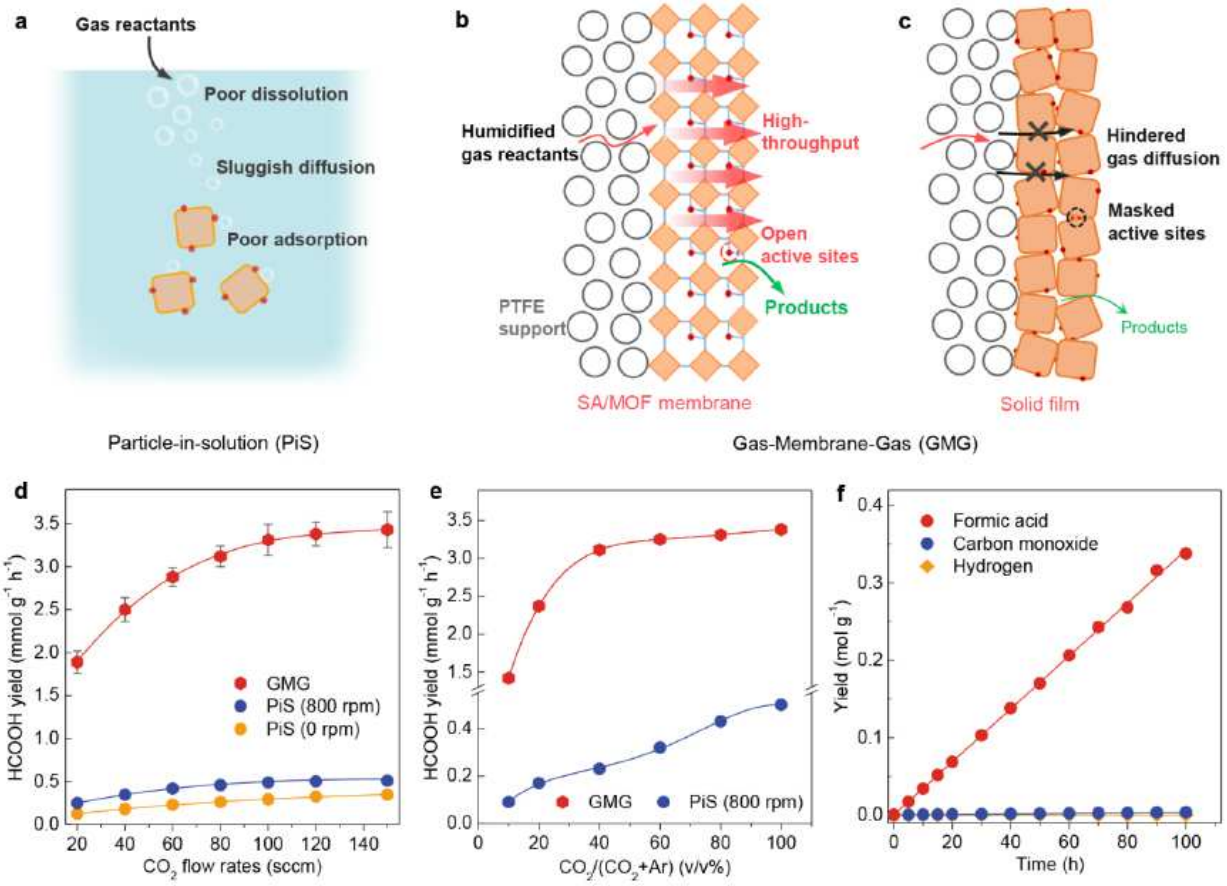

Figure 3

Photocatalytic CO2RR on SA/MOF membranes. (a) In the particle-in-solution (PiS) mode, gas-phase CO2 was fed into the aqueous photocatalyst dispersion and then reduced on the water flooded surfaces of catalysts. (b) In the gas-membrane-gas (GMG) mode, humidified CO2 gas was fed through the SA/MOF membrane, where water vapor was carried by the CO2 stream. (c) Schematic illustration for the solid films fabricated by non-porous semiconductor particles. (d) HCOOH yields on Ir1/d-aUiO particles (PiS) and membrane (GMG) under different CO2 flow rates, respectively. (e) HCOOH yields on Ir1/d-aUiO particles (PiS) and membrane (GMG) under different CO2 concentration (in Ar mixtures), respectively. (f) Time course of HCOOH, CO and H2 evolution on Ir1/d-aUiO membrane (GMG). All the photocatalytic reactions were performed under visible light (> 420 nm). The CO2 flow rates in (e) and (f) were fixed at 120 sccm. Error bars represent the standard deviation for three independent catalysis tests.

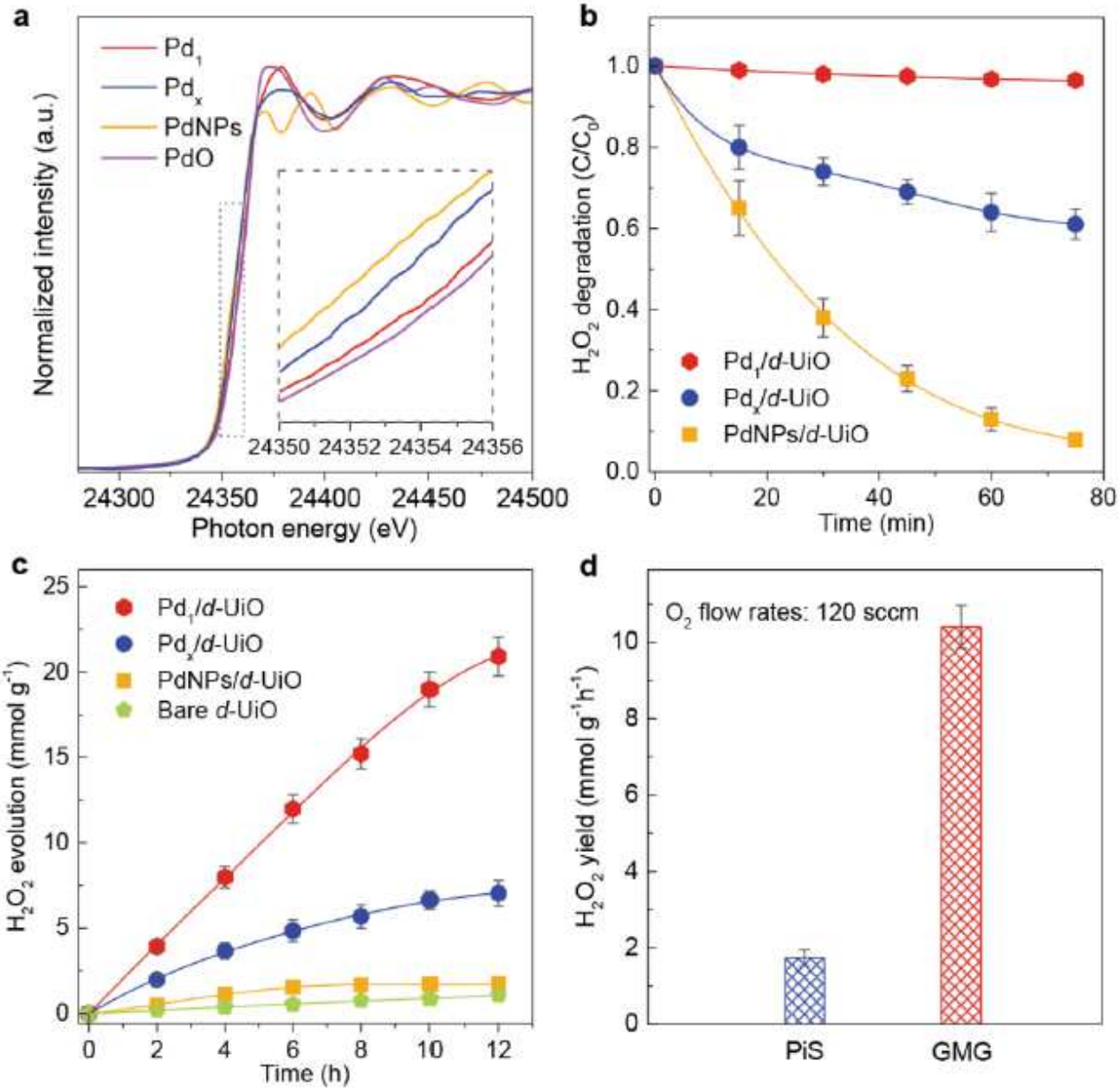

Figure 4

Photocatalytic O2 reduction (ORR) on Pd modified MOF powders and membrane. (a) Pd K-edge XANES spectra of PdNPs, Pdx and Pd1 decorated d-aUiO catalysts. PdO was used as standard. (b) Time course of H2O2 decomposition on PdNPs, Pdx and Pd1 decorated d-aUiO catalysts. (c) Time course of H2O2 generation on pristine d-aUiO and PdNPs, Pdx and Pd1 decorated d-aUiO catalysts. (d) H2O2 yields on Ir1/d-aUiO particles (PiS) and membranes (GMG), respectively. All the photocatalytic reactions were performed under visible light (> 420 nm) irradiation and using isopropanol (20 v/v% in water) as sacrificial agents. The O2 flow rates were fixed at 120 sccm. Error bars represent the standard deviation for three independent catalysis tests.

Supplementary Files

This is a list of supplementary files associated with this preprint. Click to download.

- SI.pdf